Properties of embedded convection in warm-frontal mixed-phase cloud from aircraft and polarimetric radar

By ROBIN. J. HOGAN[1]*, P. R. FIELD[2], A. J. ILLINGWORTH[1], R. J. COTTON[2] and T. W. CHOULARTON[3]
[1]*University of Reading, UK*
[2]*Met Office, UK*
[3]*UMIST, Manchester, UK*

SUMMARY

Results are presented from a case study in which the macrophysical and microphysical characteristics of a warm-frontal mixed-phase cloud were investigated using simultaneous aircraft and polarimetric radar measurements. A region of embedded convection was located and sampled at various stages of its ascent through the cloud from $-5°C$ to $-11°C$, and evidence is presented that it was triggered by Kelvin-Helmholtz instability near the melting layer. High concentrations of small crystals were observed in and above narrow convective turrets, around 1 km across, that contained supercooled liquid water droplets with an effective diameter of 24 μm and riming ice particles. The area surrounding the turrets was found to contain pristine columns, and was strikingly visible to the radar as a broad plume of high differential reflectivity Z_{DR} (around 3 dB), contrasting with the 0–0.5 dB range usually found in ice clouds. The columns observed *in situ* had axial ratios of around 5:1, in close agreement with the values predicted theoretically from Z_{DR} assuming horizontal alignment of the crystals. We argue that the high concentrations of small ice crystals (up to 10^3 1^{-1}) observed in this case were splinters produced via the Hallett-Mossop mechanism in the riming process, and these then grew rapidly by deposition in the water-saturated environment into pristine columns. Later in the ascent the picture was complicated by the presence of a fallstreak containing large, low-Z_{DR} aggregates which appeared to rapidly accrete the columns. A number of plumes of high Z_{DR} were observed by the radar on the same day, each of which persisted for at least half an hour. In the vicinity of cloud top ($-15°C$), the regions of high Z_{DR} tended to spread out horizontally, and attain values as high as 7 dB. At these temperatures plates and dendrites are known to grow, so these Z_{DR} observations are in good agreement with our theoretical finding that columns alone cannot produce values of Z_{DR} greater than 4 dB, no matter how extreme their axial ratios, whereas planar crystals can attain values up to 10 dB. Embedded convection could clearly be important in determining the distribution of ice and liquid water in frontal clouds, which affects both cloud glaciation and the radiation budget, and is important for aircraft icing.

KEYWORDS: Mixed phase   Hallett-Mossop   Differential reflectivity   Pristine crystals   Kelvin-Helmholtz

1. INTRODUCTION

Fronts are responsible for the bulk of the precipitation that falls in the mid-latitudes, and most current forecast models (which typically have horizontal resolutions between 15 km and 60 km) assume that this 'large-scale' precipitation is formed by a uniform distribution of ice particles within the model grid box which grow by deposition and aggregation as they fall, finally melting to produce rain. It is known from aircraft measurements that ice particle concentrations in stratiform clouds are often far in excess of typical ice nucleus concentrations at cloud top (Hobbs 1974; Heymsfield 1977; Hobbs and Rangno 1985; Bower *et al.* 1996), implying that some kind of ice multiplication must be taking place. Ice splinter production during riming (Hallett and Mossop 1974), known to occur in glaciating cumulus, has been suggested as a means by which high concentrations of ice crystals may be generated in stratiform clouds (Bower *et al.* 1996; Mason 1998). However, this mechanism would only be able to act in very localised regions of 'embedded convection' where the vertical velocities are sufficient to sustain the supercooled liquid water necessary for riming, and grow droplets larger than around 25 μm in diameter (Mossop and Hallett 1974). If present, these regions could clearly be important in determining the distribution of ice and liquid water within the cloud, and therefore affect both its radiative properties and the amount

---

* Corresponding author address: Department of Meteorology, Earley Gate, PO Box 243, Reading RG6 6BB, UK. E-mail: r.j.hogan@reading.ac.uk.
© Royal Meteorological Society, 2002.

of precipitation produced. Although measurements of localised updraughts containing supercooled water are not uncommon in stratiform clouds, it is very difficult to get an idea of the three-dimensional nature and evolution of embedded convection from one-dimensional aircraft penetrations alone. Consequently, parameterisations in many operational models simply assume that ice and liquid water are uniformly mixed within each gridbox, and that the ice/liquid-water ratio varies as a function of temperature alone (Smith 1990; Sundqvist 1993; Moss and Johnson 1994). Obviously this is a gross oversimplification, both in view of the fact that the coexistence of ice and liquid water particles is fundamentally unstable with the ice tending to grow at the expense of the liquid water, and because the same relationship is usually applied to mixed-phase clouds of entirely different types, such as supercooled stratocumulus, altocumulus, frontal nimbostratus and deep convection. More recently, parameterisations have been developed with separate variables for ice and liquid water that make use of model parameters such as vertical velocity to achieve a more physically based representation of mixed-phase clouds (Tremblay *et al.* 1996; Wilson and Ballard 1999). In view of the apparent sensitivity of mean model cloud amount and the associated radiation budget to the specification of mixed-phase clouds (Gregory and Morris 1996; Fowler and Randall 1996), these approaches are clearly in much need of evaluation by high-resolution observations.

In this paper, simultaneous remote and *in situ* measurements by the Chilbolton 3-GHz polarisation-diversity radar and the UK Met Office C-130 aircraft are used to study the evolution of narrow convective plumes within a warm-frontal cloud. Particular attention is paid to the radar differential reflectivity (Z_{DR}) parameter, and for the first time it is demonstrated that high values of Z_{DR} (in excess of 3 dB) in stratiform ice clouds tend to be associated with the presence of supercooled liquid water. Assuming that free-falling particles are aligned preferentially in the horizontal, Z_{DR} is essentially a measure of hydrometeor axial ratio, although in the case of ice particles it is also approximately proportional to the density of the ice-air mixture. Clearly the liquid water droplets are too small to contribute significantly to the radar signal themselves, so the implication is that ice crystals in the presence of liquid water are able to grow rapidly by vapour deposition in the supersaturated environment to form highly aspherical pristine columns, plates or dendrites. Usually ice clouds have low values of Z_{DR} (0–0.5 dB), indicating the presence of particles either without extreme axial ratios (such as bullet rosettes), or of low density and therefore low dielectric constant (such as aggregates). Indeed, Korolev *et al.* (2000) recently found from an extensive study of aircraft microphysical measurements in stratiform ice clouds that 84% of ice particles larger than 125 μm were irregular, and the relatively uncommon columns and dendrites tended to occur in cells with a characteristic scale of hundreds of metres to tens of kilometres embedded within much larger zones of irregularly shaped particles. To produce large pristine crystals with high Z_{DR} requires depositional growth to dominate over aggregation. This can occur near cloud top where aggregation has not had time to act; hence Z_{DR} in the uppermost 500 m of ice clouds is typically larger than that in the bulk of the cloud, although is usually still only around 1 dB at cloud top. When cloud top temperature is around -15°C, however, it is not uncommon to see much higher values of Z_{DR} in this region. This phenomenon was first commented upon by Hall *et al.* (1984), who observed values of 4 dB at cloud top that decreased steadily to 0.3 dB, 1 km below, and attributed them to highly asymmetric pristine ice crystals that slowly aggregated as they fell through the cloud. Sauvageot *et al.* (1986) found that in stratiform ice clouds, Z_{DR} was more likely to be greater than 2 dB at -12°C than at any other temperature above the melting layer. Hogan *et al.* (1999) presented observations of a warm-frontal

ice cloud with Z_{DR} values up to 6 dB due to the presence of pristine sector plates, and from simultaneous airborne lidar measurements showed them to be associated with a thin layer of liquid water at cloud top, where the temperature was $-15°$C. This suggests that by maintaining high supersaturations, the presence of supercooled liquid can cause crystals near cloud top to grow much more rapidly into pristine forms than would otherwise be the case.

The high-Z_{DR} features associated with embedded convection that are described in this study occur in the *middle* of the cloud, so it would seem that a source of large numbers of small crystals, which initially at least are too small to aggregate, is required to explain the phenomenon. We present evidence to show that these small crystals are most likely to be splinters thrown off large riming snowflakes or graupel (which are themselves distinctly visible to the radar) via the Hallett-Mossop mechanism for secondary ice production (Hallett and Mossop 1974). Observations of similar embedded high-Z_{DR} features, together with colocated *in situ* measurements of ice crystal shape, have been published by Liu and Herzegh (1986) and Bader *et al.* (1987), but were not accompanied by measurements of liquid water or the suggestion that either liquid water or ice multiplication played a part in their formation. Note also that high values of Z_{DR} have been observed at temperatures down to $-10°$C in strongly convective storms, but these were shown to be caused by small numbers of very large supercooled raindrops carried aloft in strong updraughts (Illingworth *et al.* 1987), and could not be present in the relatively quiescent stratiform clouds considered in this paper.

In section 2 we describe the ground-based and airborne measurement techniques used in the paper, and outline how differential reflectivity is related to crystal shape and alignment. The radar and aircraft observations are described in section 3 and interpreted in section 4.

2. DESCRIPTION OF MEASURED PARAMETERS

(a) Radar reflectivity factor and differential reflectivity

The fundamental parameter measured by radar is reflectivity factor (Z), and for a unit volume containing homogeneous spherical particles it is given by

$$Z = \sum_i \frac{|K_i|^2}{0.93} D_i^6, \tag{1}$$

where D is diameter and $|K|^2$ is the 'dielectric factor' of the particle, which for liquid water is 0.93 and for solid ice is 0.17. Because of the presence of the sixth power of diameter, Z tends to be dominated by the contribution of the larger particles, which in mixed-phase clouds are invariably the ice particles. However, the effective bulk density of most ice particles (particularly aggregates) is significantly less than that of solid ice, and one should invoke Debye's theory (Battan 1973) in which $|K|$ is proportional to the bulk density of the ice-air mixture. According to the relationship of Brown and Francis (1995), the bulk density of irregular ice particles is approximately inversely proportional to their maximum dimension. Thus, in ice, Z is often approximately proportional to the fourth power of particle diameter rather than the sixth.

If the particles are non-spherical and are aligned such that they extend more in the horizontal dimension than the vertical, then the reflectivity factor measured at horizontal polarisation, Z_H, will be greater than that at vertical, Z_V. Hence differential reflectivity
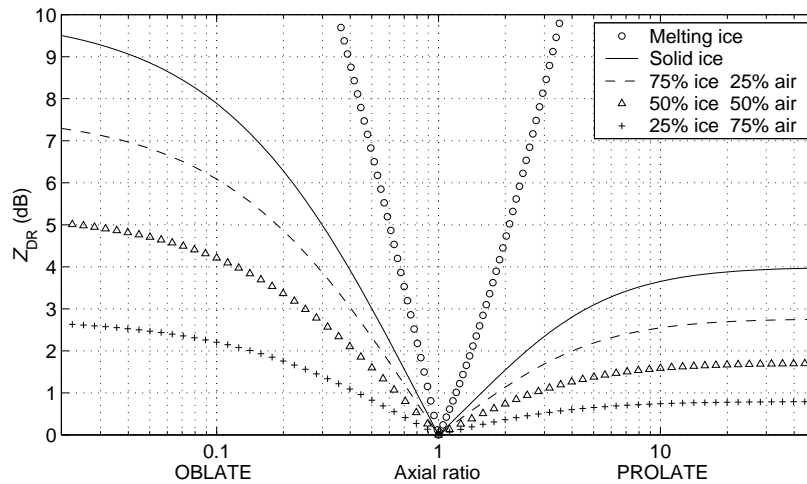
Figure 1. Z_{DR} of spheroidal ice particles as a function of axial ratio and density. The particles are horizontally aligned but have random azimuthal orientation.

(Z_{DR}), expressed in conventional logarithmic units as

$$Z_{DR} = 10 \log_{10} \left(\frac{Z_H}{Z_V} \right) \ \ dB, \tag{2}$$

is a measure of hydrometeor shape and alignment in the radar pulse volume (Seliga and Bringi 1976). It is commonly used in rain to improve rain-rate estimates because of the unique relationship between raindrop shape and size, but in ice its interpretation is much more ambiguous since ice particles occur in a multitude of different habits which are generally not related to size. Furthermore, the Z_{DR} of ice particles (in dB) is approximately proportional to their effective density. This is particularly important for aggregates which, as far as the radar is concerned, consist largely of air and thus tend to have a Z_{DR} close to 0 dB. The effective density of pristine crystals, however, is much closer to that of solid ice, so large values of Z_{DR} are possible. Clearly any tumbling or canting would reduce Z_{DR}, but it is well established that free-falling ice crystals tend to lie with their longest axis in the horizontal (Cho *et al.* 1981; Pruppacher and Klett 1997; Liou 1986).

The Z_{DR} of horizontally oriented plates and columns has been calculated as a function of axial ratio and density and is shown in Fig. 1. Details of the calculation may be found in the appendix. We have approximated plates as oblate spheroids and columns as prolate spheroids, which is reasonable because it is the induced dipole that is important in the Rayleigh-scattering regime; the higher multipoles that are needed to describe the precise crystal shape do not radiate efficiently. Curves are plotted for solid ice and for three different homogeneous ice-air mixtures, using the formula of Meneghini and Liao (1996) to calculate the effective dielectric constant from the ice-air ratio. An interesting finding is that, no matter how extreme the axial ratio, the Z_{DR} of non-melting plates cannot exceed 10 dB and the Z_{DR} of columns cannot exceed 4 dB. A practical problem to bear in mind is that large, low-density aggregates, even if present in relatively low concentrations, could dominate the reflectivity, thereby masking the effect of the smaller pristine crystals on Z_{DR} (Bader *et al.* 1987). We discuss the likely impact of this effect when analysing our data. Also shown in Fig. 1 is the Z_{DR} of melting plates

and columns, calculated assuming that, with a coating of liquid water, the particles have the same dielectric constant as liquid water.

In this paper we use the 3-GHz Chilbolton Advanced Meteorological Radar in Southern England. The large antenna (25 m diameter) affords both high sensitivity and a very narrow beam ($0.28°$). Illingworth *et al.* (1987) showed that the narrow beam enables it to avoid the problem of high Z_{DR} being erroneously generated by sidelobe effects (Herzegh and Conway 1986). In addition to its polarisation capability, we also make use of its ability to measure the radial component of the wind when cloud or precipitation is detected. The capabilities of the instrument were described in full by Goddard *et al.* (1994).

(b) *Aircraft* in situ *measurements*

The UK Met Office Hercules C-130 is well equipped to measure the microphysical properties of mixed-phase clouds. Bulk liquid water content (LWC) is provided by a Johnson-Williams hot-wire probe, which together with the Nevzorov total condensed water probe allows ice water content (IWC) to be measured (Korolev *et al.* 1998). Three Particle Measuring System (PMS) instruments are available to measure the full particle size distribution. The 2D cloud and precipitation probes (hereafter '2D-C' and '2D-P') nominally measure hydrometeors in the diameter ranges 25–800 μm and 200–6400 μm respectively, and are based on the instrument described by Knollenberg (1970). They operate by illuminating a linear array of 32 photodiodes and as particles pass through the system they occlude the beam and a two-dimensional image is compiled from which shape and size can be determined. Although the minimum size measurable by the 2D-C probe is nominally 25 μm, the work of Baumgardner and Korolev (1997) indicates that, due the low response time of optical array probe electronics, the smallest particle that could be sized at aircraft speeds of 100 m s^{-1} (the typical speed of the C-130) would be closer to 50 μm. Their analysis considered only spheres and it is unclear how the results would differ for non-spherical ice particles. The PMS Forward Scattering Spectrometer Probe (FSSP) counts particles in the diameter range 2–47 μm, although because over-counting of small particles may occur when large ice crystals are present (Gardiner and Hallett 1985), we only use concentrations measured by this instrument qualitatively.

3. OBSERVATIONS

(a) *Synopsis*

The case study took place on 30 March 1999 as part of the UK Natural Environment Research Council 'Clouds, Water Vapour and Climate' thematic programme. The flight strategy was for the C-130 to fly straight and level search runs at around the $-5°C$ level along a radial to the west of Chilbolton until a good candidate convective region was encountered, typically with a vertical velocity of around 0.5 m s^{-1} at the same time as at least 0.1 g m^{-3} of liquid water. Then the aircraft would commence an ascending 'Lagrangian' figure-of-eight pattern centred on the region as it advected towards the north east, consisting of a series of 2-min straight and level runs (around 12 km in length) separated by climbs of around 150 m. During the course of the flight three such regions were located and tracked, although only the second of the ascents was particularly successful.

Figure 2 shows the Met Office surface analysis at noon, in which we see a waving front extending over the south of the UK. According to the operational radar network this was associated with light stratiform precipitation of around 1 mm hr^{-1} that persisted
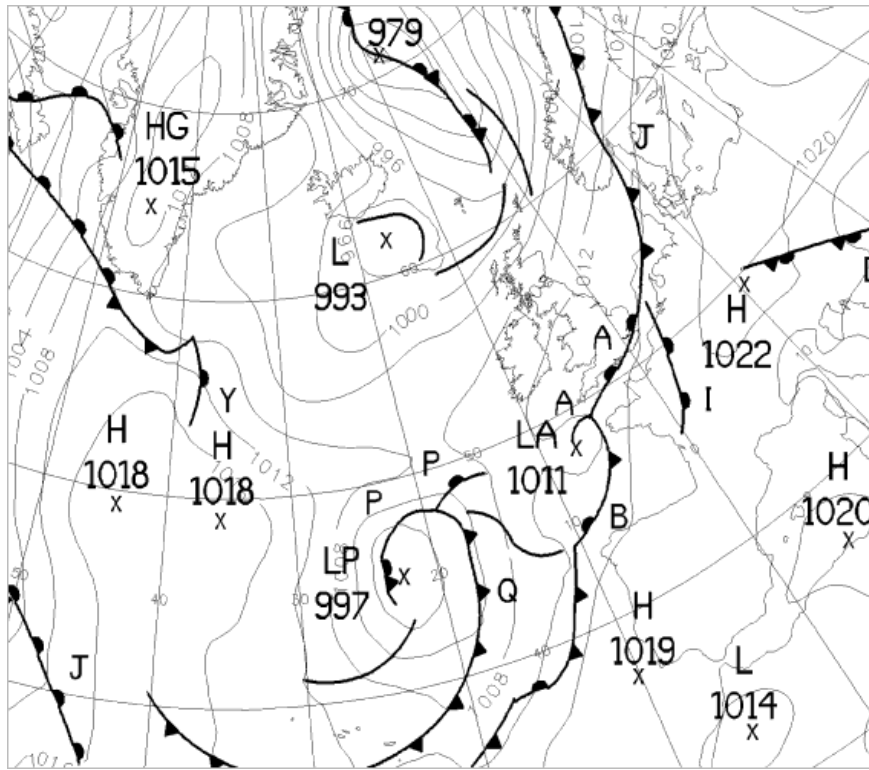
Figure 2.   UK Met Office surface analysis at 1200 UTC on 30 March 1999.
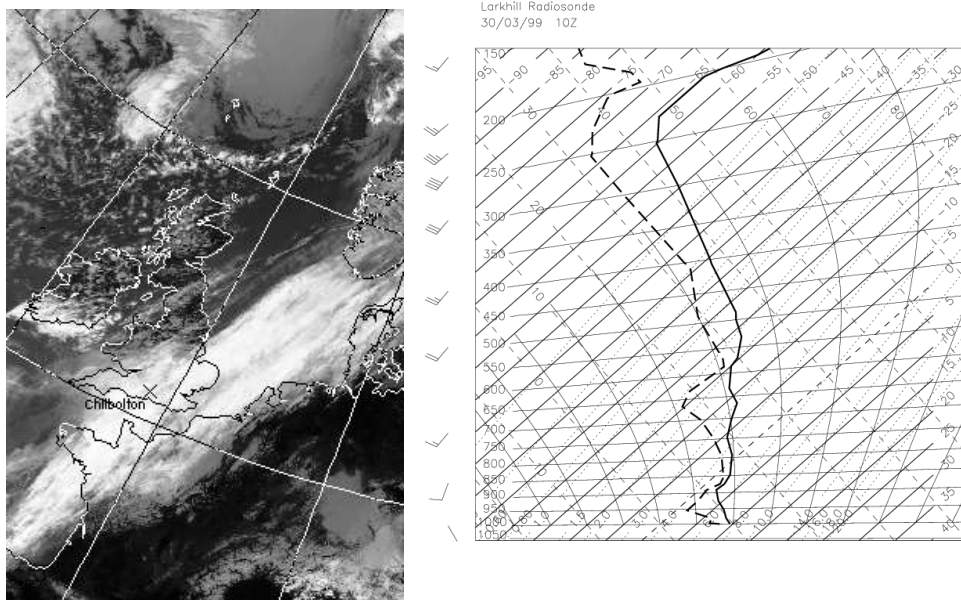

Figure 3.   Infrared satellite image from the Advanced Very High Resolution Radiometer at 1335 UTC, and the Larkhill radiosonde ascent at 1000 UTC, on 30 March 1999.

TABLE 1. SUMMARY OF THE AIRCRAFT RUNS IN THE 1214–
1244 UTC LAGRANGIAN ASCENT ON 30 MARCH 1999. RUN 18
WAS ABANDONED DUE TO AIR TRAFFIC RESTRICTIONS.

Run	Time (UTC)	Altitude (km)	Mean temperature (°C)
17	1214	2.75	−5.1
19	1222	2.90	−6.1
20	1225	3.06	−7.1
21	1228	3.22	−8.4
22	1232	3.37	−9.4
23	1236	3.52	−10.0
24	1240	3.67	−10.7
25	1244	3.81	−11.5

for most of the day. During the period of the experiment the cloud was continuous up to around 5.5 km. Figure 3 shows the 1335 UTC infrared satellite image and the 1000 UTC radiosonde ascent from Larkhill, in which we see a layer at −15°C close to saturation with respect to liquid water. Larkhill is located 25 km to the west of Chilbolton, very close to the flight path of the aircraft.

(b) *The 1214–1244 UTC Lagrangian ascent through embedded convection*

We first discuss the second of the three Lagrangian aircraft ascents, which was the most successful since the aircraft managed to stay centred on the main region of embedded convection as it rose from −5°C to −11°C during the 30-min period. The eight runs of the ascent are summarised in Table 1, and Fig. 4a shows the flight track of the aircraft relative to Chilbolton for each run. Figures 4b–4f show the mean values of a number of different parameters measured by the aircraft during each run, together with the 20th and 80th percentiles. Each 12 km run only partially intercepted the convective core (which as shall be seen later was less than 2 km wide), so the 80th percentile provides an estimate of the values associated with the convective region. All parameters were found to reach a maximum during run 22 (3.37 km, −9.4°C) except IWC and ice concentration which both peaked during run 23 (3.52 km, −10.0°C).

As the aircraft ascended, the radar performed both horizontal and vertical scans through its position. For each run, the nearest radar scan (in time) has been found, and to account for any remaining time differences, has been shifted horizontally using the mean wind measured by the aircraft (around 17 m s^{-1} from the 215° direction). In practice the nearest suitable scan in time to each aircraft run was never more than a few minutes away, and the scans were not moved further than 3 km. The nearest radar pixel to each point along the aircraft flight track was then located and the corresponding values of Z and Z_{DR} extracted.

Figure 5 shows the vertical radar scans of radial velocity, Z and Z_{DR} for four of the aircraft runs through the region of embedded convection. Superimposed on these are the aircraft measurements of vertical velocity, IWC and LWC respectively. Note that the radar azimuth increased from 245° to 269° during this period in order to track the position of the aircraft, and since the wind was coming from the 215° direction, the evolution of features cannot be precisely followed from one scan to the next at all heights. We first consider the radar velocity and Z patterns. The slanted 'fallstreak' structure is evident in most of the ice region, and is explained by the vertical shear of around 5 m s^{-1} km^{-1} that is evident in the radar velocity data. This structure was advected by the mean wind from right to left (approximately west to east) at a rate of around 1 km min^{-1}. Note that the apparent undulations of cloud top are probably an
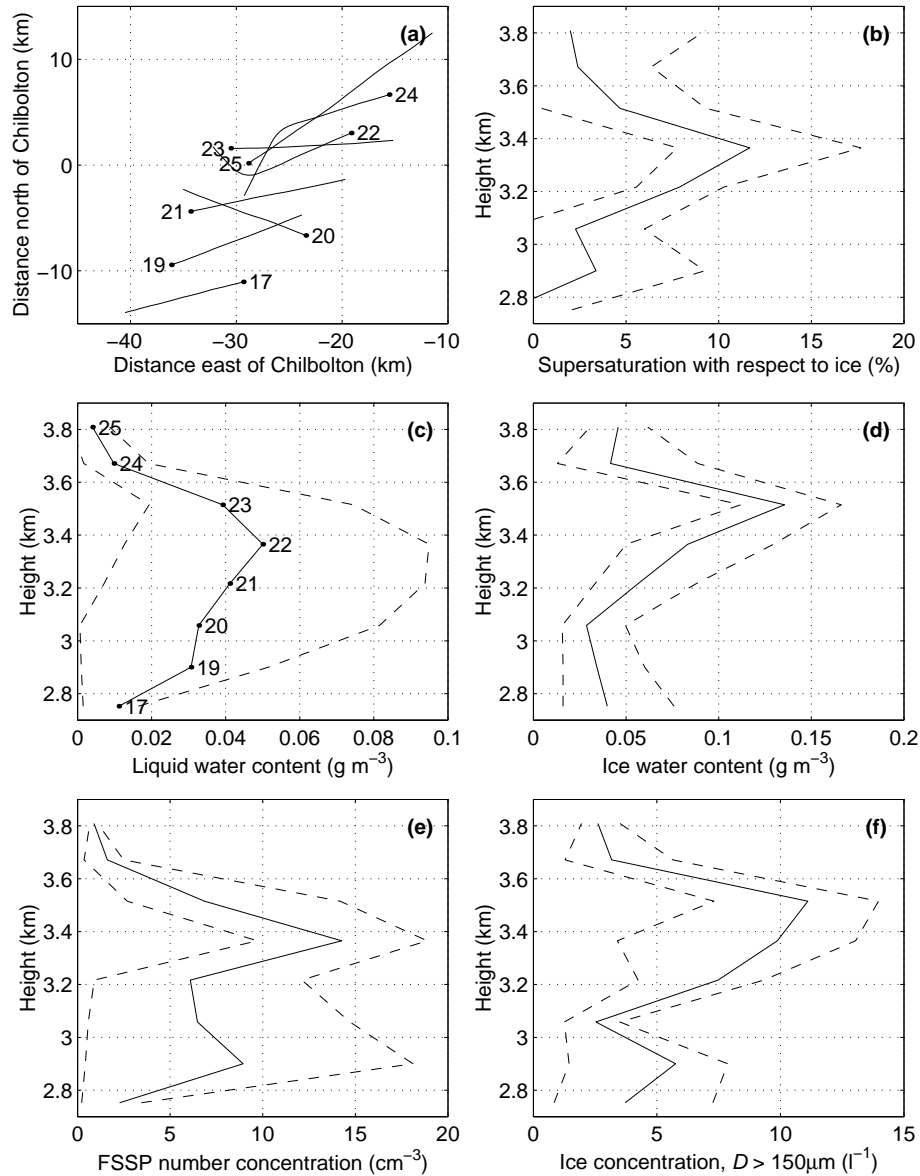
Figure 4.   Panel a depicts the flight track of the aircraft relative to Chilbolton for runs 17 to 25 (indicated at the start of each track) of the 1214–1244 UTC ascent, and panels b to f show the mean values of five variables measured during each run (solid lines), together with the 20th and 80th percentiles (dashed lines). The variables are: supersaturation with respect to ice, liquid water content, ice water content, FSSP number concentration and the combined 2D-C and 2D-P concentration of particles larger than 150 μm (which we assume to be ice).

artifact of the limited sensitivity of the radar; the depressions in cloud top tend to occur in the gaps between the tops of fallstreaks where Z is too low to be detected.

The presence of a pronounced bright band at 1.8 km indicates that the melting particles were aggregated, low-density snowflakes; if they were heavily rimed then as melting commenced the increase in dielectric constant (and therefore Z) would have been much less, and when they melted completely into rain the reduction in size would
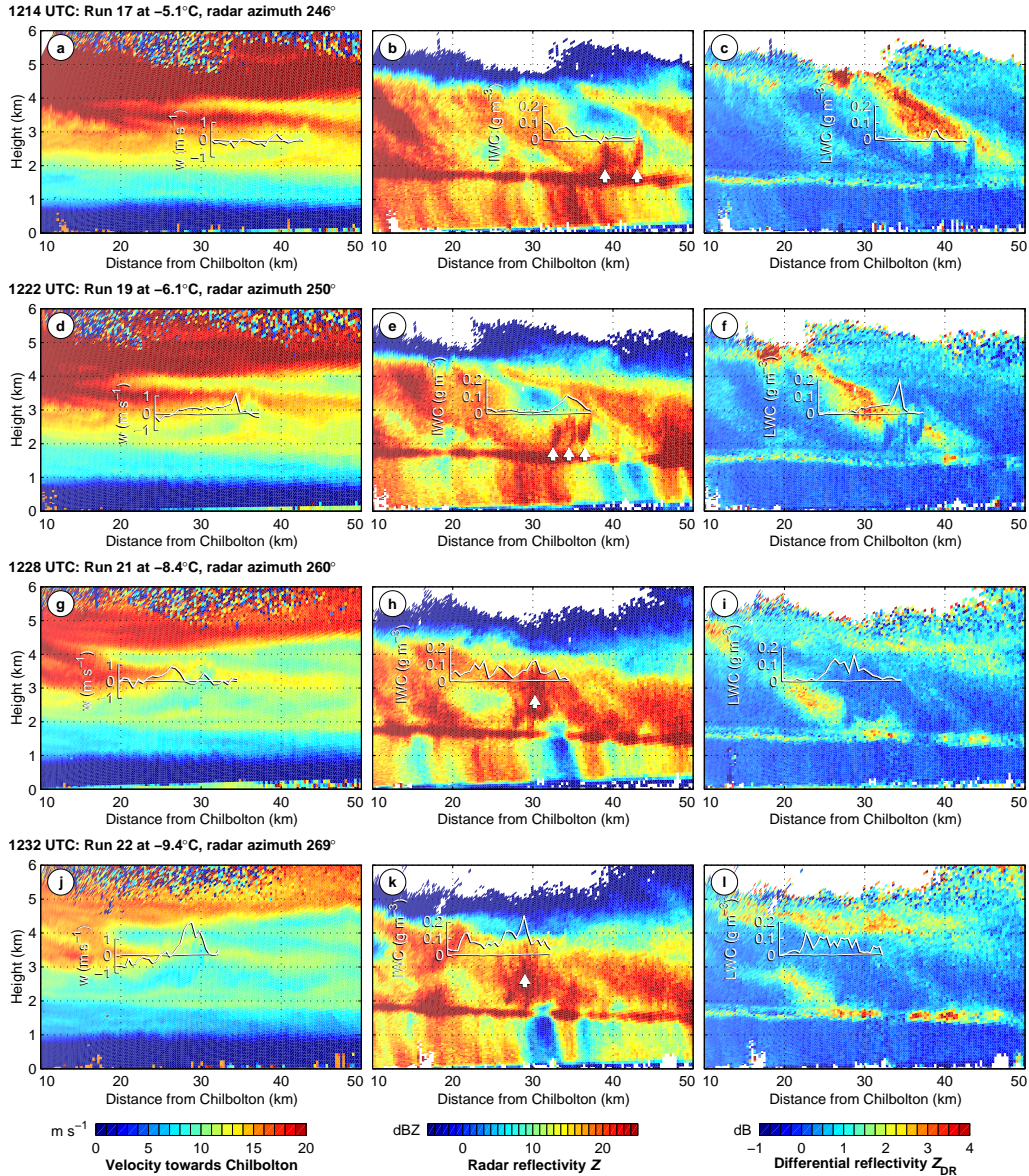
1214 UTC: Run 17 at −5.1°C, radar azimuth 246°

1222 UTC: Run 19 at −6.1°C, radar azimuth 250°

1228 UTC: Run 21 at −8.4°C, radar azimuth 260°

1232 UTC: Run 22 at −9.4°C, radar azimuth 269°

Figure 5. Vertical radar scans of radial velocity, Z and Z_{DR} for aircraft runs 17, 19, 21 and 22 through embedded convection. Superimposed on the scans are the aircraft measurements of vertical velocity (w), IWC and LWC. Positive radial velocities are towards the radar.

also have been much smaller. The Z values in the rain range between 0 and 25 dBZ, corresponding to surface rain rates of between 0.02 and 1.5 mm hr^{-1}. However, in the vicinity of the aircraft it is the narrow upright 'turrets' of high Z (marked by the arrows) that are most striking. In run 17, two are distinctly visible at a range of 39 and 43 km, each measuring approximately 1 km×1 km. The nearer of the two to Chilbolton is clearly associated with a cell of slowly ascending supercooled liquid water that was measured by the aircraft as it flew just above the turret. These turrets are apparent in the later scans at higher levels in the cloud, and can also be seen to distinctly perturb
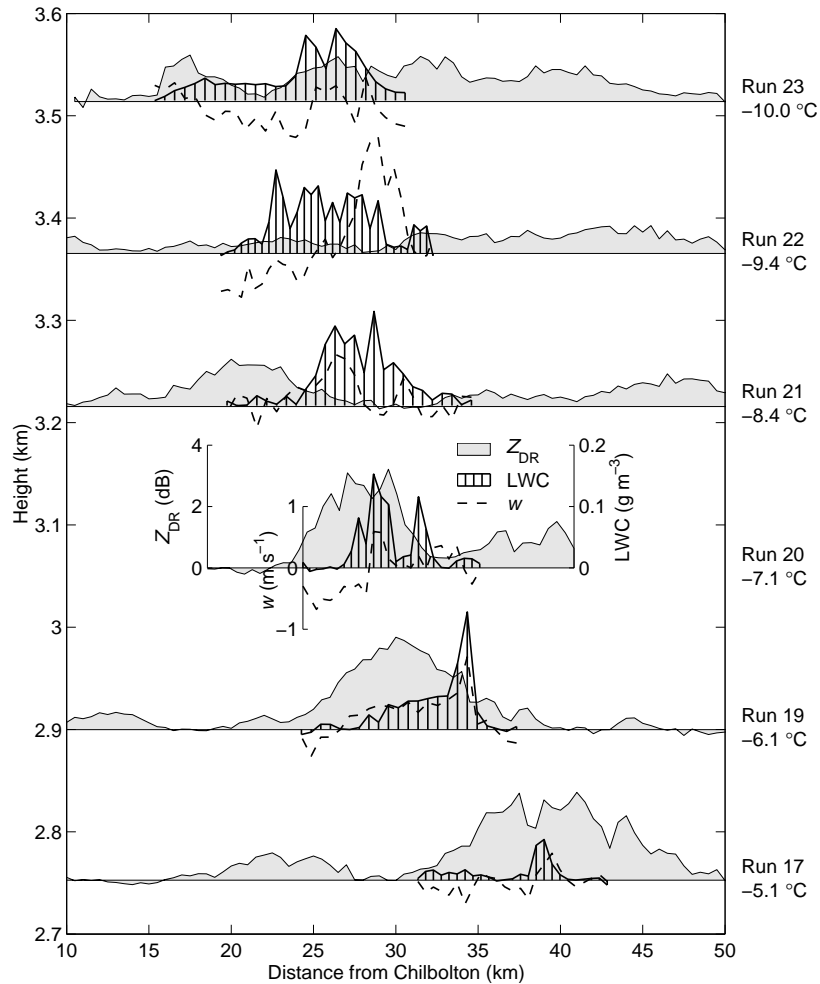
Figure 6.   Cross-sections of Z_{DR}, LWC and vertical velocity (w) during the 1214–1244 UTC ascent, compiled from 6 aircraft runs at temperatures between $-5.1°C$ (run 17) and $-10.0°C$ (run 23). Z_{DR} was extracted from vertical scans in all runs except 20, where the only suitable scan was horizontal at an elevation of $5.5°$. Thus in this case the height at which Z_{DR} was sampled is not constant with range.

the horizontal velocity pattern (Figs. 5g and 5j). The aircraft seems to have stayed well centred on them from one run to the next, where it measured peak vertical velocities of 1–2 m s^{-1}, LWCs of 0.1–0.15 g m^{-3} and IWCs of 0.1–0.2 g m^{-3}.

We next consider the Z_{DR} images in Fig. 5. The dominant feature of the first two scans (in which the aircraft was at $-5.1°C$ and $-6.1°C$ respectively) is the slanted plume of high Z_{DR} (up to 4 dB), around 5 km across, extending from a little above the melting layer all the way to cloud top. In the next section we will show that this is due to the presence of pristine crystals growing by deposition in the supersaturated environment. The two convective turrets identified in the Z images are visible here as regions of $Z_{DR} = 0$ dB, which appear to be rising into the high-Z_{DR} plume. This indicates that the particles responsible for the high-Z turrets were quasi-spherical, and given the availability of supercooled water droplets in the ascending air it seems likely that they were riming snowflakes or maybe even small graupel pellets. Figure 6 summarises the

comparison of radar Z_{DR} with aircraft LWC and vertical velocity for runs 17 to 23 (after which the aircraft and radar data were not well enough matched in space for a valid comparison). The high-Z_{DR} plume appears to decay as it is advected to the east between runs 17 and 21, and by run 22 has virtually disappeared (see also Fig. 5l), although this is partially due to it moving out of the plane of the vertical scans. The ascending region of supercooled liquid water tends to stay to the western side (i.e. at a greater range from Chilbolton) of the high-Z_{DR} region and broaden somewhat. By run 23 the Z_{DR} appears to be increasing again, and from Figs. 5i and 5l it would seem to be the lower edge of a developing layer of elevated Z_{DR} near cloud top, directly above the embedded convection. We can interpret this as being due to unaggregated ice particles near cloud top that undergo rapid growth by deposition when liquid water ascends into the region from below and spreads out horizontally. Since the temperature is below $-9°$C here, pristine plates and dendrites will form. The radiosonde ascent in Fig. 3 indicates the presence of near liquid water saturation at the $-15°$C cloud top, and in principle a thin layer of liquid water could persist here in much the same manner as altocumulus, maintained by cellular overturning driven by radiative cooling to space. The aircraft ascent in this case was abandoned after run 25 so the region was unfortunately not sampled above 3.81 km. Hogan *et al.* (1999) also observed high-Z_{DR} radar signals at the $-15°$C top of a frontal cloud, and using data from an airborne lidar showed them to be associated with a thin but horizontally extensive liquid water layer. In section 3e, observations of larger values of Z_{DR} at cloud top are presented.

An interesting feature of Fig. 5l is the increased Z_{DR} (to around 5 dB) at the melting layer to each side of the embedded convection. In stratiform precipitation Z_{DR} is always observed to rise to 1–2 dB in the melting layer as low-density snowflakes with modest axial ratios acquire a coating of liquid water and their effective dielectric constant increases, before they melt completely into spheres with a Z_{DR} close to 0 dB. If instead the melting particles were pristine crystals with large axial ratios then when they start to melt they would have a significantly higher Z_{DR}. According to Fig. 1, a Z_{DR} of 5 dB in the melting layer could be caused by horizontally aligned melting columns with an axial ratio of 2, or plates with an axial ratio of 0.6.

(c)   *Detailed* in situ *measurements from run 19*

We now examine and compare the aircraft and radar data from runs 19 and 22 in more detail. During run 19 the characteristics of both the embedded convection and the high-Z_{DR} region surrounding it were sampled. Figure 7 shows the variables measured simultaneously by the radar and the aircraft during this run and Fig. 8 shows samples of images from the 2D-C and 2D-P probes measured at evenly spaced intervals through the run.

At this altitude the aircraft was just skimming the top of the high-Z turret 34 km from Chilbolton (Fig. 5e), so was ideally positioned to sample any small crystals produced by the riming particles beneath. In Fig. 7 we see that a number of the variables exhibited a 'spike' around 1-km wide, immediately above the embedded convection; here LWC reached 0.19 g m^{-3} (its highest value at temperatures below 0°C for the entire flight), IWC was around 0.1 g m^{-3}, the vertical velocity was 1 m s^{-1} and the droplet effective diameter measured by the FSSP was 24 μm. There was also an abundance of small ice particles; the combined number concentration measured by the 2D-C and 2D-P probes (i.e. all particles larger than around 50 μm in diameter) reached 2500 l^{-1}, more than two orders of magnitude larger than the values a mere 5 km closer to Chilbolton. Some of these particles may have been liquid water droplets, but even the concentration
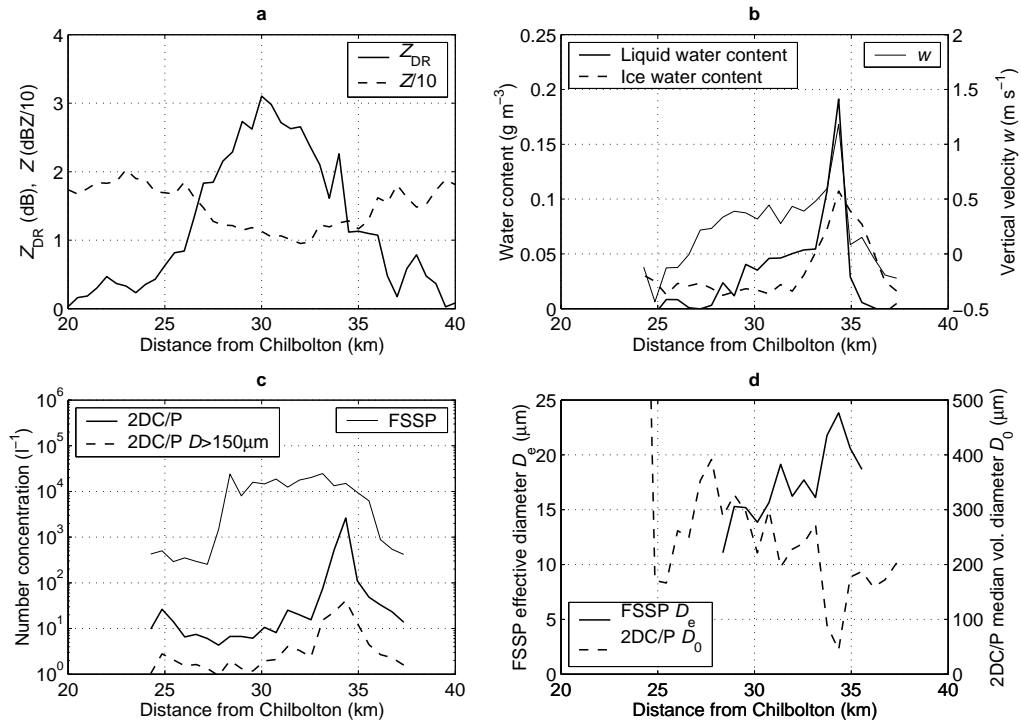
Figure 7.   Variables measured by the radar (panel a) and the aircraft (panels b-d) at 1222 UTC during run 19. FSSP effective diameter has only been plotted where the FSSP number concentration exceeded $2000\,l^{-1}$.

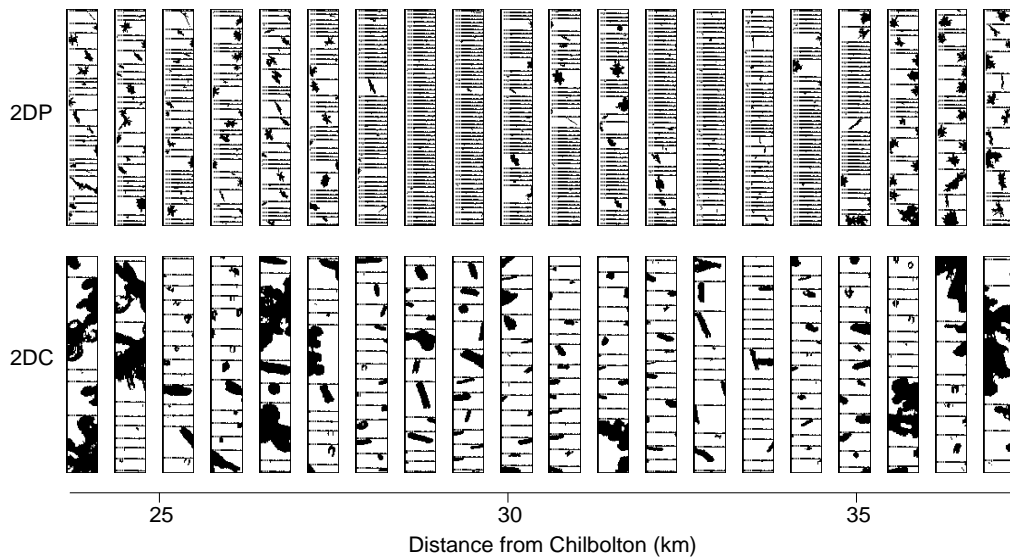Figure 8.   Some of the crystal images sampled by the 2D-C (25–800 μm) and 2D-P (200–6400 μm) probes at evenly spaced intervals during run 19, between 24 and 37 km from Chilbolton. They correspond to the bulk data plotted in Fig. 7.

of particles larger than 150 μm was around 40 l^{-1}, which is still around five orders of orders of magnitude larger than the typical concentrations of ice nuclei at $-6°$C, and approaching three orders of magnitude higher than the likely values at cloud top (Fletcher 1962). Therefore some form of ice multiplication must have been responsible. The Hallett-Mossop mechanism would seem to be the most likely candidate seeing as the peak in concentration coincided with the presence of droplets with a diameter larger than 25 μm, and occurred directly above a region believed to contain riming particles in the -3 to $-8°$C temperature range. Other possible mechanisms, such as break-up on evaporation (Oraltay and Hallett 1989; Bacon *et al.* 1998) or fracture due to ice-ice collision (Vardiman 1978; Griggs and Choularton 1986), would be unable to produce the observed horizontal narrowness of the peak in concentration.

Calculations have been performed of the growth of particles within the water-saturated updraught region using the one-dimensional model of Cardwell and Choularton (2000). This model includes a full description of secondary ice particle production by the Hallett-Mossop process. These show that in the water-saturated environment splinters will reach a size detectable by the 2D-C probe after about 1 minute of growth. Hence with an updraught of 1 m s^{-1} these will have been emitted about 60 m below the observation level for run 19, close to the region where the rate of production splinters during the riming process would be expected to be a maximum of 200 splinters per milligram of accreted water. Particles larger than 150 μm were also observed at the level of the aircraft in much lower concentrations and these would be expected to be about 6 mins old and have an origin in the temperature range of $-3°$C to $-4°$C. In this temperature range the rate of production of splinters is much less than the peak value but is still significant (declining rapidly to zero at $-3°$C). Hence the observed enhanced number concentrations of ice particles in the updraught region are quantitatively consistent with the operation of the Hallett-Mossop process just below run 19.

We next look at the cause of the broader high-Z_{DR} region that occurred to either side of the convective turrets in Fig. 5f. The 2D-P images in Fig. 8 show the presence of snowflakes up to 2 mm in size, except between around 27 and 35 km from Chilbolton where typical sizes were only a few hundred microns. This absence of larger particles explains the 10 dB reduction in Z that is apparent in Figs. 5e and 7a. The 2D-C images indicate the presence of numerous 500 μm columns in this area, with axial ratios of around 5:1. It is well known that columns grow in the temperature range $-3°$C to $-9°$C, so these crystals must have grown in the middle of the cloud rather than falling from cloud top. The apparently random alignment of the columns in the images is due to local acceleration as the crystals were drawn into the probe (Gayet *et al.* 1993). From Fig. 1 we see that a distribution of horizontally aligned solid columns with axial ratios of 5:1 and random azimuthal orientation should produce a Z_{DR} of 3 dB, which is indeed the value that was measured. The horizontal extent of the high-Z_{DR} coincides closely with that of a broad region of supercooled liquid water droplets (with an LWC of around 0.05 g m^{-3}, a number concentration of around 1.5×10^4 l^{-1} and an effective diameter of 14–19 μm) ascending at around 0.4 m s^{-1}.

The ice concentrations in the high-Z_{DR} region (around 10 l^{-1}) were comparable to the 'ambient' concentrations measured throughout the experiment, and to concentrations commonly reported in the literature. Despite being two orders of magnitude lower than the 10^3 l^{-1} measured in the embedded convection, this value is still itself two orders of magnitude larger than the 0.1 l^{-1} that would be expected from primary nucleation alone. If Hallett-Mossop ice multiplication associated with embedded convection was effective in, say, 1% of a long-lived cloud, then mixing with the surroundings could explain the

elevated concentrations in the rest of the cloud at a level two orders of magnitude below the values in the convective turrets themselves. Equally, it is quite possible that one or more of the other ice multiplication mechanisms could be operating continuously throughout the entire cloud (albeit at a much slower rate than Hallett-Mossop), thereby raising the ambient ice concentration above the cloud-top ice nucleus concentration.

(d)   *Detailed* in situ *measurements from run 22*

From the Z images of Fig. 5 it is clear that during run 19 the embedded convection was rising into a gap between two fallstreaks, but by run 22 it had penetrated one of them. Figure 9 shows the radar and aircraft variables measured during run 22, and Fig. 10 shows a sample of the corresponding crystal images. In run 19 the aircraft was skimming the tops of the high-Z/low-Z_{DR} turrets which we suggested could contain riming particles, but in run 22 the aircraft actually penetrated the top of a turret at a temperature of $-9.4°$C. As in run 19, a 'spike' was observed in many of the aircraft parameters at the same location as the turret indicated by the radar reflectivity (28 km from Chilbolton); here IWC peaked at 0.22 g m^{-3}, vertical velocity was 1.9 m s^{-1} and the concentration of particles larger than 150 μm reached 50 l^{-1}. The corresponding median volume diameter measured by the combined 2D-C and 2D-P probes was 250 μm, and in the 2D-C images 27.5 km from Chilbolton it appears that these particles were quasi-spherical ice pellets which had probably grown by riming. The process of riming would soon lead to graupel too large to be carried up in the modest updraughts that were observed, so 'sorting' by size is likely to have occurred, with the large graupel and riming snowflakes tending to occur lower down in the high-Z region. Unfortunately the aircraft did not penetrate the base of the embedded convection to verify this. It is interesting that the highest concentration of particles measured by the combined 2D-C and 2D-P probes occurred 3 km downstream, 25 km from Chilbolton, where the concentration was 1000 l^{-1} (somewhat less than the maximum value in run 19). Here the median volume diameter was only 50 μm. These observations are consistent with the Hallett-Mossop hypothesis; at $-9.4°$C riming in the convective core would no longer release splinters, but splinters produced several hundred metres below would still be carried aloft in the weaker updraughts of the surrounding air. Since the horizontal wind is sheared with height, a separation could have occurred once the Hallett-Mossop became inactive, with the splinters in the weaker updraughts drifting downstream relative to the convective core which produced them. The high concentrations of small quasi-spherical ice particles in the convective core indicates that they may themselves have originated as splinters. The supercooled liquid at this altitude was no longer concentrated in the convective core, but spread over a 7 km region downwind of it, with water contents of 0.05–0.1 g m^{-3}.

Z_{DR} was much lower during run 22 at the altitude of the aircraft than in run 19, due to the fact that the embedded convection was by this time penetrating a fallstreak containing large, low-density irregular ice particles. Bader *et al.* (1987) suggested that this limited the applicability of Z_{DR} for detecting pristine crystals with extreme axial ratios, because their intrinsic Z_{DR} could so easily be masked by the presence of larger aggregates at much lower concentrations. Masking does not appear to be occurring in this case, because the the 2D-C images of Fig. 10 indicate the presence of large irregular particles, but no columns are evident. Thus we conclude that any columns carried up in the broad 0.4 m s^{-1} updraught observed in run 19 were rapidly aggregated on entering the fallstreak. Similarly, any newly formed splinters carried aloft into the fallstreak would be unlikely to grow by deposition to any significant size before being aggregated.
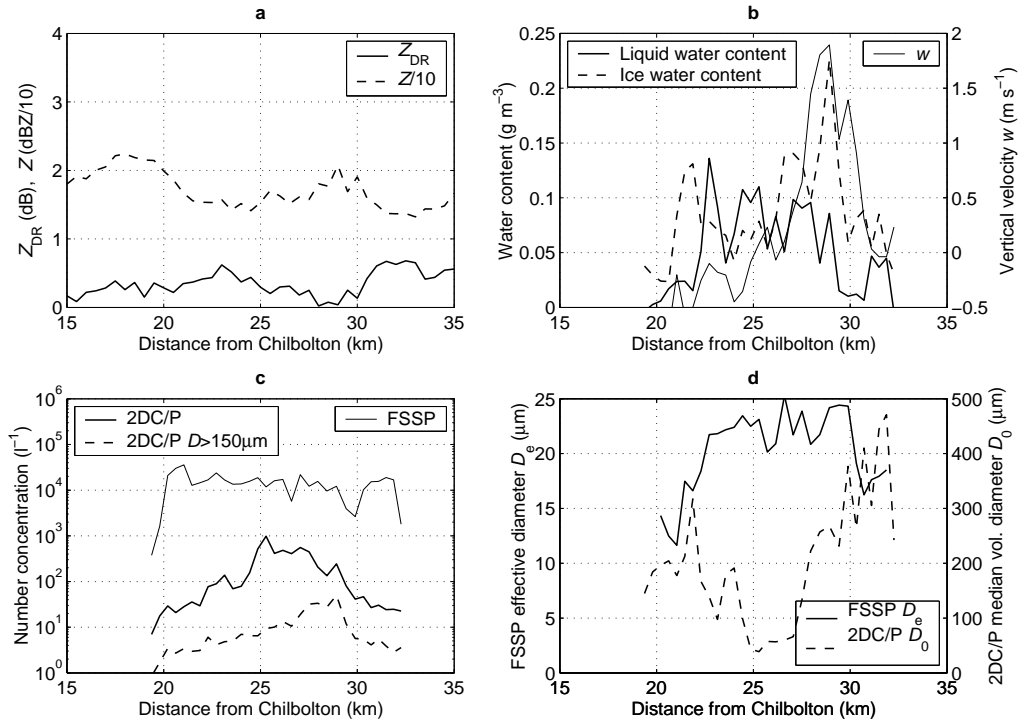
Figure 9. Variables measured by the radar (panel a) and the aircraft (panels b-d) at 1232 UTC during run 22. FSSP effective diameter has only been plotted where the FSSP number concentration exceeded $2000\,\mathrm{l}^{-1}$.
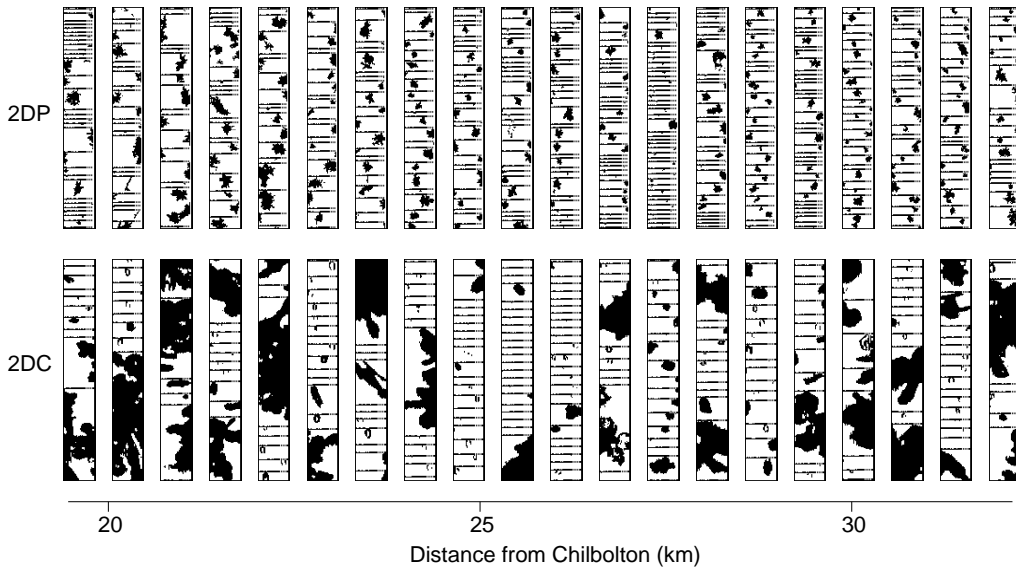

Figure 10. Crystal images measured by the 2D-C and 2D-P probes at evenly spaced intervals during run 22, corresponding to the bulk data shown in Fig. 9.
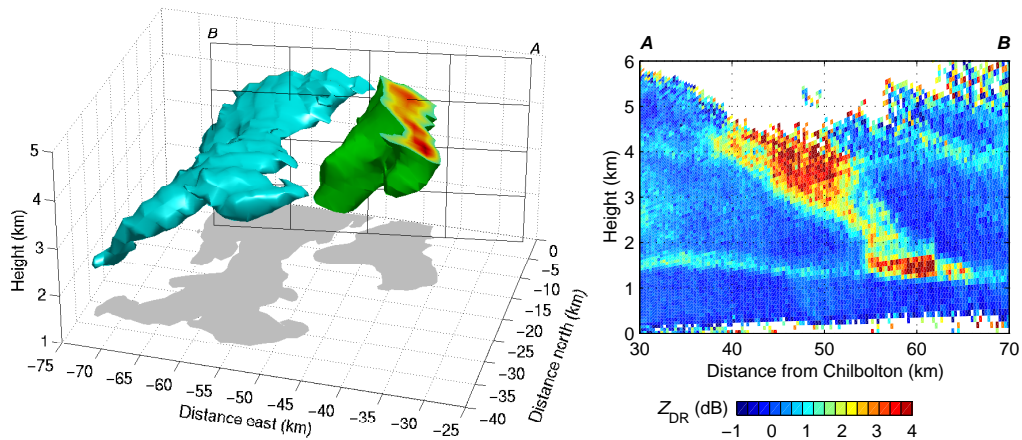
Figure 11.   The left plot depicts the $Z_{DR} = 2$ dB isosurface at 1135 UTC (blue) and 1157 UTC (green), as derived from two 'volume scans', each consisting of 6 horizontal scans at elevations between $0.5°$ and $5.5°$. The black wire frame shows the plane of a horizontal scan taken at 1152 UTC, which is shown reversed in the right panel.
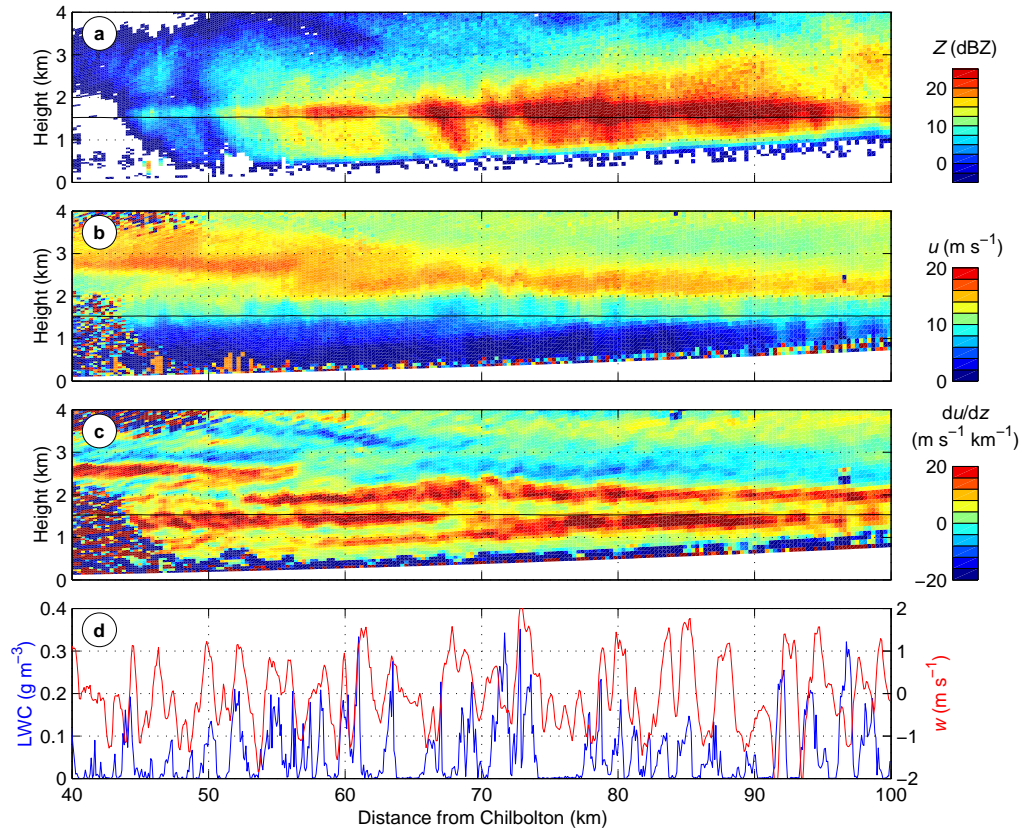
Figure 12.   Radar and aircraft measurements in Kelvin-Helmholtz billows between 1030 and 1041 UTC, along the $270°$ radial. The panels are (a) radar reflectivity, (b) radar radial velocity, (c) vertical wind shear derived from the radial velocity, and (d) simultaneous aircraft measurements of LWC and vertical velocity (w) at an altitude of 1.53 km. The solid horizontal line on each radar scan indicates the position of the aircraft, where the temperature ranged between 0 and $2°$C.

(e)   The longevity and spatial distribution of high-Z_{DR} plumes

A number of high-Z_{DR} plumes were observed by the radar during the flight, although only the one described in the last section was adequately sampled by the aircraft. Earlier in the flight a plume was sampled by only the radar as it was advected in from the south west over a 30-min period. The highest Z_{DR} measured during this period was 7 dB at cloud top, which according to Fig. 1 must have been caused by plates or dendrites. At 1135 UTC and 1157 UTC 'volume scans' were performed, consisting of 6 horizontal scans at elevations between 0.5° and 5.5°. From these it was possible to reconstruct the three-dimensional Z_{DR} field; the 2 dB isosurface of Z_{DR} is shown in Fig. 11 at the two times, together with a vertical scan taken shortly before the second volume scan. At 1135 UTC we see a layer of $Z_{DR} > 2$ dB at cloud top (4 km), with an east-west extent of 10 km and a north-south extent of at least 35 km. Beneath the layer a plume around 5 km across extended in a slantwise fashion down to the melting layer. Twenty-one minutes later the plume had been advected around 25 km to the north east and had broadened somewhat. Unfortunately the horizontal scans at the later time did not extend high enough to characterise the full extent of the layer, although the vertical scan shows it to still extend around 10 km in the east-west direction. It would seem likely that the high-Z_{DR} region at cloud top was associated with supercooled liquid water collecting there, and it is interesting that the horizontal extent of this layer is comparable to the typical horizontal scales reported by Hogan and Illingworth (1999) for thin supercooled liquid water clouds detected in three years of ground-based lidar data. Possibly the high-Z_{DR} plumes could have been fed by embedded convective events, but none of the scans exhibited the same high-Z turrets (attributable to riming ice particles) that were described in the previous section; it is possible that they were present but were missed by the scan sequence because of their small size. In the right panel of Fig. 11, as in Fig. 5l, values of Z_{DR} up to 5 dB are present at the base of the plume where the pristine crystals were melting. The fact that this feature was present throughout the 30-min period suggests that the high-Z_{DR} plume was already quite mature, and the riming event which produced the necessary splinters may have occurred well before the radar began scanning through it.

(f)   The role of Kelvin-Helmholtz waves

An interesting feature of the velocity images of Fig. 5 (particularly panels d and g) is the presence of a train of low-amplitude (50–100 m) Kelvin-Helmholtz waves with a wavelength of around 2 km at an altitude of 1 km. These were observed many times during the period that the radar was scanning in this case study (0800–1400 UTC) and were sampled *in situ* at 1030 UTC when the aircraft performed a run at an altitude of 1.53 km, close to the melting level. The results are depicted in Fig. 12. The radar radial velocity (panel b) shows waves similar in wavelength and amplitude to those observed in Fig. 5, associated with strong fluctuations in both aircraft LWC and vertical velocity, with peak values of around 0.25 g m^{-3} and ± 1.5 m s^{-1} respectively. Horizontal scans indicated that the waves were oriented approximately north-south, so this east-west transect should provide an accurate indication of their wavelength. The wind shear in Fig. 12c (derived from the radial velocity) is concentrated in two layers at 1.5 and 2 km, where the magnitude reached 20 m s^{-1} km^{-1}. Chapman and Browning (1997) reported radar observations of Kelvin-Helmholtz billows in a warm-frontal zone with an amplitude of 500 m, and, by assuming two-dimensional flow limited to the plane of the vertical radar scan, estimated them to be associated with updraughts of up to
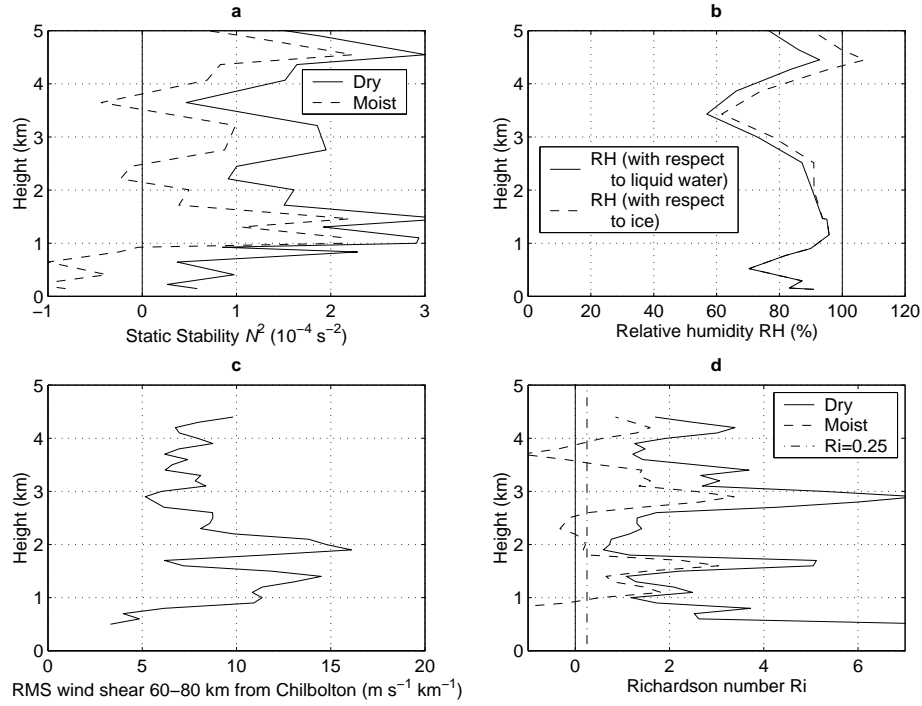
Figure 13. Larkhill radiosonde data at 1000 UTC and radar observations at 1040 UTC: (a) radiosonde dry and moist static stability, (b) radiosonde relative humidity, (c) rms shear of the radar radial velocity between 60 and 80 km from Chilbolton, and (d) dry and moist Richardson Number derived from the static stability and rms wind shear.

$3 \, \mathrm{m \, s^{-1}}$. They showed that the split shear structure was the result of the action of Kelvin-Helmholtz waves on an initial single layer of high wind shear.

Although Z_{DR} was not especially high during this time, clearly vertical velocities of this magnitude could have been responsible for triggering the embedded convection that was observed later in the flight, and appeared to have originated from near the melting layer. Kelvin-Helmholtz instability is known to occur when the Richardson Number (Ri), defined as the ratio of the static stability N^2 to the square of the vertical wind shear, is less than $\frac{1}{4}$. We now estimate the magnitude of Ri using the temperature profile from the 1000 UTC radiosonde ascent shown in Fig. 3, together with the radar observations of wind shear. When air is unsaturated the static stability is given by

$$N^2 = \frac{g}{T} \left(\frac{dT}{dz} - \Gamma_d \right), \tag{3}$$

where T is temperature, z is height, g is the gravitational acceleration and Γ_d is the dry adiabatic lapse rate. When the air is saturated, however, it is of the form (Lalas and Einaudi 1974):

$$N^2 = \frac{g}{T} \left(\frac{dT}{dz} - \Gamma_m \right) \left(1 + \frac{Lq_s}{RT} \right) - \frac{g}{1 + q_w} \frac{dq_w}{dz}, \tag{4}$$

where Γ_m is the saturated adiabatic lapse rate, L is the latent heat of evaporation, R is the ideal gas constant for dry air, q_s is the saturation mixing ratio and q_w is the total water

mixing ratio. Since the vertical distribution of liquid water depends on the history of the motion of individual air parcels, which is generally unknown, we follow Durran and Klemp (1982) and make the approximation $\partial q_w/\partial z \approx \partial q_s/\partial z$. Figure 13a shows the dry and moist static stabilities derived from the 1000 UTC radiosonde ascent, and Fig. 13b depicts the corresponding relative humidity profile. The air appears to be potentially unstable but unsaturated below the warm-frontal surface at 1 km, and close to saturation and stable from 1 to 2 km. At 1000 UTC the cloud field according to the radar was much more intermittent (particularly between 2 and 4 km) than at 1040 UTC when the data in Fig. 12 were taken. In the intervening time, large-scale frontal ascent presumably brought the layer between 1 and 2 km to saturation. The Kelvin-Helmholtz waves in Fig. 12b are most pronounced at a range of 70 km from Chilbolton, so this is where we calculate Ri. Figure 13c shows the rms shear of the zonal wind measured by the radar between 60 and 80 km from Chilbolton, with the corresponding dry and moist Richardson Numbers in Fig. 13d. Between 1.9 and 2.1 km the moist Ri was 0.2 so here we would expect Kelvin-Helmholtz billows to develop when the air reached saturation. The billows will then have generated the strong fluctuations in liquid water content and vertical velocity that were observed by the aircraft in Fig. 12d, although ice particles falling into the layer from above could clearly have swept out some of the liquid water as soon as it formed. Chapman and Browning (1999) showed in a similar warm-frontal case how the saturation of a widespread layer undergoing frontal ascent permitted the rapid development of Kelvin-Helmholtz instability as the effective Richardson Number suddenly dropped below $\frac{1}{4}$.

Between 2.1 and 2.5 km the air was potentially unstable to moist convection, so even if the air was not saturated here, saturated parcels at the crests of the Kelvin-Helmholtz waves in the layer beneath could have found themselves lifted into an environment in which free convection was possible, and then continued to ascend in the form of the convective turrets that were observed in Fig. 5. It is even possible that the north-south orientation of the high-Z_{DR} layer at cloud top in Fig. 11 reflects the north-south orientation of the Kelvin-Helmholtz wave crests much lower in the cloud.

4. DISCUSSION AND CONCLUSIONS

Previous studies have found significantly higher ice crystal concentrations in stratiform clouds than can be explained by primary nucleation alone, and have cited the Hallett-Mossop mechanism for secondary ice production, known to be important in convective clouds, as a plausible candidate to explain the discrepancy (Hobbs and Rangno 1985, Bower et al. 1996). This process occurs only in riming conditions between -3 and $-8°$C, and so in stratiform clouds is likely to act only in very localised 'embedded convective' regions. In this paper we have presented the first detailed simultaneous remote and *in situ* measurements of such a region. We now summarise these results and discuss the merits of the Z_{DR} parameter for mapping out regions containing pristine crystals. The schematic diagram in Fig. 14 is an attempt to encapsulate our interpretation of the observations in terms of the microphysical processes that were occurring.

The embedded convection itself was identified by the radar as individual turrets (around 1 km across) of high Z and low Z_{DR}, indicating the presence of large or high-density particles, roughly spherical in shape. These turrets were found by the aircraft to be associated with similarly narrow updraughts of 1–2 m s^{-1} containing 0.1–0.2 g m^{-3} of liquid water (including 25 μm droplets) and concentrations of small ice crystals up to 2 orders of magnitude larger than the 'ambient' values only 5 km away. At $-6.1°$C the peak in ice concentration measured by the aircraft was immediately above a high-Z
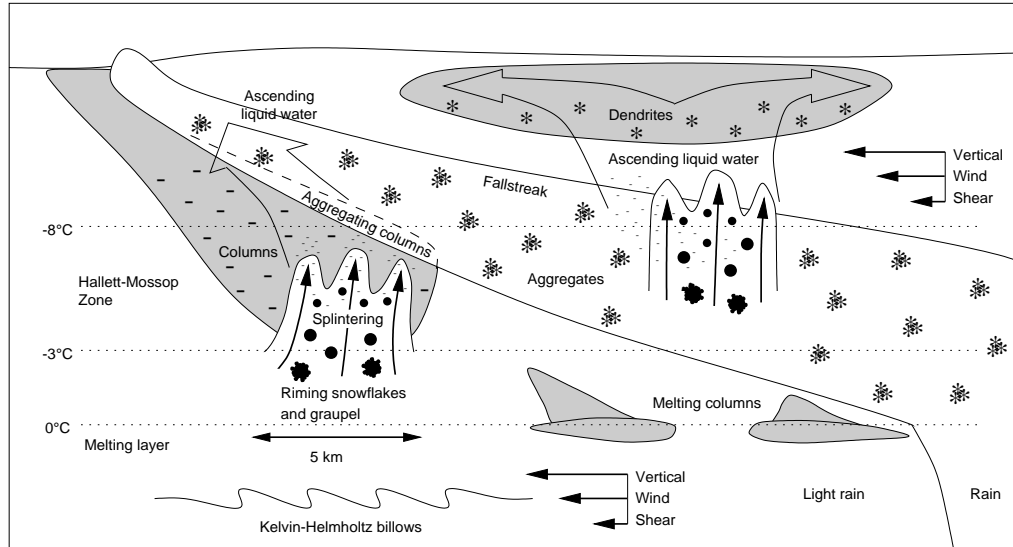
Figure 14.   Schematic showing the development of the embedded convection. The shaded areas indicate regions
of high Z_{DR} due to the presence of crystals with extreme axial ratios.

turret (Fig. 7) but by $-9.4°C$ appeared to have spread as much as 3 km downstream
(Fig. 9). This lends support to the contention that these crystals were splinters produced
from riming ice particles in the convective core via the Hallett-Mossop mechanism; no
other ice multiplication mechanism would be likely to generate such a narrow spike in
ice concentration immediately above a region where riming was occuring. Also, the fact
that the Hallett-Mossop mechanism does not operate effectively at temperatures below
$-8°C$ could explain the apparent separation of the highest ice concentrations from the
convective core by the $-9.4°C$ run. The remaining difference between the ambient ice
concentrations and the expected cloud-top ice nucleus concentration could be simply
due to mixing from a number of Hallett-Mossop plumes into the surrounding cloud,
although the possibility of additional slow but widespread ice multiplication by some
other mechanism (such as break-up on evaporation or collision) cannot be ruled out.

   Unfortunately the convective core itself was not well sampled by the aircraft until the
later runs, and even then the aircraft was only a few hundred metres below the top of the
convection as indicated by the Z field. During this penetration, near-spherical ice pellets
around 250 μm in diameter were observed at concentrations up to approximately 50 l^{-1}
(see Figs. 9c and 10). They were probably graupel in very early stages of riming, and at
this size would have had a terminal velocity of only around 0.4 m s^{-1} (Mitchell 1996),
allowing them to be carried up by the updraught. Their high concentration suggests that
they themselves did not originate from primary nucleation alone. Presumably a sorting
by size would occur with the larger graupel (on which we assume most of the splintering
to have taken place) falling back through the cloud.

   One of the most interesting aspects of the early radar scans was the presence of a
slanted region of elevated Z_{DR}, around 5 km across, which extended from the immediate
vicinity of the convective turrets up to cloud top. From the radar images in Fig. 5
alone this feature has the superficial appearance of a 'fallstreak' of some kind, and
it is not clear that it is even related to the high-Z turrets; their proximity could be
coincidental. Furthermore, the intensity of the Z_{DR} plume appears to diminish and

become disassociated with the embedded convection in the later scans (Figs. 5i and 5l). However, the *in situ* evidence indicates that the high-Z_{DR} region is intimately associated with the nearby embedded convection, and that it is not a fallstreak in the normal sense. Aircraft sampling near the base of the high Z_{DR} ($-6.1°$C) showed it to contain pristine columns growing in a modest updraught of around 0.4 m s^{-1} with LWC at around 0.05 g m^{-3}. The presence of pristine columns in the middle of a cloud that otherwise consists of aggregates requires a source of reasonable concentrations of small 'seed' crystals which can then grow by deposition. These particular columns cannot simply have fallen from near cloud top in the manner of a fallstreak since at temperatures below $-9°$C (400 m higher up in the cloud) the predominant depositional growth mode is planar. Also, crystals nucleated near cloud top falling through a water-saturated updraught would be much larger than the columns observed by the time they reached the $-6.1°$C level. Thus the most likely scenario is that splinters produced by the Hallett-Mossop mechanism were ejected from the top of the ascending convective turrets (since their terminal velocity was so much less than graupel) and carried downstream of the convection by the shear of the horizontal wind. In the more modest vertical velocities surrounding the convection, the liquid water content was too low for significant riming to occur, yet the air was still supersaturated with respect to ice so in the absence of larger aggregates the splinters were able to grow by deposition into the columns that were observed. The radar scans in Figs. 5c and 5f indicate that high Z_{DR} extended all the way to the apparent cloud top at 5 km; presumably this was fed by a water-saturated updraught that had existed for some time, with depositional growth of plates or dendrites at upper levels.

So why was the embedded convection no longer surrounded by a high-Z_{DR} region in the later radar images? It must in part have been due to the fact that the high-Z_{DR} feature moved out of the plane of the radar scans as the radar attempted to stay centred on the aircraft while it was tracking the embedded convection. By this time the convection was penetrating a fallstreak containing large, low-density aggregates, and it is noticeable in the first two runs of Fig. 5 how areas of high-Z_{DR} lie exclusively in low reflectivity regions. There is also a distinct anticorrelation of Z and Z_{DR} evident in Figs. 7a and 9a. Bader *et al.* (1987) suggested that a widespread problem for the interpretation of differential reflectivity signatures was that the presence of a few large aggregates was sufficient to 'mask' the intrinsic high-Z_{DR} of any pristine crystals present. However, there is simply no evidence of columns in the crystal images observed by the aircraft in run 22 (Fig. 10), or indeed in any of the runs after 19. This is despite the presence of similar concentrations of small ice particles and high supersaturations with respect to ice. So it seems reasonable to suppose that the pristine columns were simply accreted by the aggregates. This would suggest that Z_{DR} is in fact a reasonable proxy for the presence of pristine crystals, and the fact that high values of Z_{DR} were found exclusively in low-Z regions merely reflects the fact that pristine crystals tend not to coexist with aggregates. Hence the slanted appearance of the high-Z_{DR} feature would seem to be due not to it being some kind of fallstreak, but to the confinement of the pristine crystals in a gap between regions of larger aggregates, which are themselves falling in a slantwise manner in the sheared environment. Presumably the slanted high-Z_{DR} plume tracked in section 3e over a 30-min period was similarly confined in a gap between fallstreaks of aggregates.

Further aircraft and radar experiments are currently in progress to explore the prevalence of embedded convection and Hallett-Mossop splintering within warm fronts. The ability of the radar to detect the presence of pristine crystals, which appears to

be a tell-tale signature of the phenomenon (particularly when they occur in the middle of the cloud), should enable the aircraft more easily to locate potentially interesting areas. From a large number of horizontal scans in this study we estimate that at the altitudes at which the Hallett-Mossop mechanism can act, around 5% of the cloud by area had a Z_{DR} exceeding 2 dB, although detailed analysis of a single high-Z_{DR} plume suggests that perhaps in only a tenth of this area were vertical velocities sufficient for riming and splinter production. The continued transport of liquid water to cloud top also warrants further investigation, particularly in light of observations of widespread high-Z_{DR} and strong lidar echos near cloud top (Hogan *et al.* 1999; Hogan and Illingworth 1999), which suggest that liquid water may collect there and persist for long periods. Modelling work is currently in progress to examine how periodic embedded convective events affect the distribution of ice water within stratiform clouds, and ultimately their effect on frontal rainfall and development (Cardwell and Choularton 2000).

APPENDIX

Here we show how the Z_{DR} measured by a Rayleigh-scattering radar (for which the scatterers are much smaller than the wavelength) at low elevations is related to ice particle axial ratio. For the problem to be tractable analytically it is necessary to approximate columns as internally homogeneous prolate spheroids and plates as homogeneous oblate spheroids. The results are plotted in Fig. 1, and are valid for a distribution of ice particles each with the same axial ratio and density, although the particles need not be the same size. It is assumed that the particles lie with their longest axis in the horizontal. We define the dimensions of an ellipsoidal particle in each of its three principal axes to be a, b and c, and for oblate particles specify that $a < b = c$ while for prolate particles we specify that $a > b = c$.

Differential reflectivity is expressed in terms of the mean backscatter cross-section at horizontal (H) and vertical (V) polarisation:

$$Z_{DR} = 10 \log_{10} \left(\frac{\bar{\sigma}_H}{\bar{\sigma}_V} \right) \text{ dB}, \tag{A.1}$$

where the mean is taken over the various azimuthal orientations of the particle. We now consider the determination of backscatter cross-sections separately for oblate and prolate particles.

(*a*)   *Oblate ice particles*

For oblate particles the calculation is straightforward because the shorter a-axis points vertically. Thus for both horizontally and vertically polarised incident beams, the incident electric field vector is parallel to one of the three principal axes of the particle, and the induced electric dipole moment will also be along this axis. The approach that follows was also taken by Seliga and Bringi (1976) to calculate the Z_{DR} of oblate raindrops, and is based on an extension to Rayleigh theory developed by Gans (1912).

The dipole moments induced in the particles for horizontally and vertically polarised beams are

$$\mathbf{p}_H = 4\pi \epsilon_0 \mathbf{E}_{H0} \, \alpha_b; \qquad \mathbf{p}_V = 4\pi \epsilon_0 \mathbf{E}_{V0} \, \alpha_a, \tag{A.2}$$

where $\mathbf{E}_{H0}$ and $\mathbf{E}_{V0}$ are the complex electric field intensities incident on the particle at the two polarisations, α_a and α_b are the polarisabilities of the particle along its a and b axes respectively, and ϵ_0 is the permittivity of free space. The backscatter cross-section

at horizontal polarisation is then

$$\sigma_{\mathrm{H}} = 4\pi \left(k^2 \frac{|\mathbf{p}_{\mathrm{H}}|}{4\pi \epsilon_0 |\mathbf{E}_{\mathrm{H0}}|} \right)^2 = 4\pi k^4 |\alpha_b|^2, \tag{A.3}$$

and similarly for vertical polarisation, where k is the wavenumber. The polarisability along the a axis is given by

$$\alpha_a = \frac{V(\epsilon - 1)}{1 + (\epsilon - 1)L_a}, \tag{A.4}$$

and similarly for the b and c axes, where V is the volume of the particle and ϵ is the relative permitivity. L_a, L_b and L_c are 'geometrical factors', and for an oblate spheroid are

$$L_a = \frac{1}{e^2} \left(1 + \frac{a/b}{e} \sin^{-1} e \right); \qquad L_b = L_c = \frac{1 - L_a}{2}, \tag{A.5}$$

where the eccentricity e is defined by $e^2 = 1 - (a/b)^2$. Thus if all the particles in the distribution have the same axial ratio we may combine (A.1) to (A.5) to obtain

$$Z_{\mathrm{DR}} = 10 \log_{10} \left(\frac{|\alpha_b|^2}{|\alpha_a|^2} \right) = 20 \log_{10} \left(\frac{1 + |\epsilon - 1|L_a}{1 + |\epsilon - 1| [1 - L_a] /2} \right). \tag{A.6}$$

In the limit of extremely oblate particles, $L_a \to 1$ and thus $Z_{\mathrm{DR}} \to 20 \log_{10} |\epsilon|$. This represents the maximum possible Z_{DR} that can be attained by ice plates. For solid ice, $|\epsilon| = 3.15$ (Liebe *et al.* 1989), and the corresponding maximum possible Z_{DR} is 10 dB.

(b) Prolate ice particles

The calculation for prolate particles is a little more complicated because the longer a axis of the particle lies in the horizontal and has a random azimuthal orientation. At vertically polarisation this is not a problem; the incident electric field vector is still parallel to one of the two other principal axes of the particle (b or c) so is independent of azimuthal orientation and we can use the same approach as for oblate spheroids. Van de Hulst (1957) gave the geometrical factors of prolate spheroids as:

$$L_a = \frac{1 - e^2}{e^2} \left(-1 + \frac{1}{2e} \ln \frac{1 + e}{1 - e} \right); \qquad L_b = L_c = \frac{1 - L_a}{2}, \tag{A.7}$$

where this time the eccentricity is defined by $e^2 = 1 - (b/a)^2$. The backscatter coefficient for vertical polarisation is simply

$$\sigma_{\mathrm{V}} = 4\pi k^4 |\alpha_b|^2. \tag{A.8}$$

At horizontal polarisation, the incident electric field vector is not necessarily parallel to one of the principal axes of the particle, so in general the induced electric dipole moment is not parallel to it either, although it will lie in the horizontal plane. Let θ be the angle between the a axis of the particle and the direction of propagation of the incident radiation. If the induced dipole moment then makes an angle ϕ with the direction of propagation of the incident radiation, we may rewrite (A.3) as

$$\sigma_{\mathrm{H}} = 4\pi \left(k^2 \frac{|\mathbf{p}_{\mathrm{H}}| \sin \phi}{4\pi \epsilon_0 |\mathbf{E}_{\mathrm{H0}}|} \right)^2. \tag{A.9}$$

This expresses the well-known 'dumb-bell' shaped Rayleigh scattering pattern. Since $|\mathbf{p}_H| \sin \phi$ is simply the component of $\mathbf{p}_H$ parallel to the incident electric field $\mathbf{E}_{H0}$, we need not calculate ϕ from θ explicitly. We can consider the induced dipole to be the vector sum of dipoles induced independently along the a and b axes (both of which lie in the horizontal plane). Considering only the components parallel to $\mathbf{E}_{H0}$, we have

$$|\mathbf{p}_H| \sin \phi = 4\pi \epsilon_0 |\mathbf{E}_{H0}|(\alpha_a \sin^2 \theta + \alpha_b \cos^2 \theta). \tag{A.10}$$

Note that both the initial induction of the dipole, and the subsequent evaluation of its component parallel to $\mathbf{E}_{H0}$, produce a dependence on θ, resulting in the squared sine and cosine terms in (A.10). Substitution into (A.9) results in

$$\sigma_H = 4\pi k^4 \left(|\alpha_a|^2 \sin^4 \theta + |\alpha_b|^2 \cos^4 \theta + 2|\alpha_a||\alpha_b| \sin^2 \theta \cos^2 \theta \right). \tag{A.11}$$

At this stage we need to calculate the average backscatter cross-section for a distribution of prolate particles with random azimuthal orientation θ by integrating with respect to θ and dividing by 2π:

$$\bar{\sigma}_H = 4\pi k^4 \left(\frac{3}{8}|\alpha_a|^2 + \frac{3}{8}|\alpha_b|^2 + \frac{1}{4}|\alpha_a||\alpha_b| \right). \tag{A.12}$$

Combining this with (A.1), (A.4) and (A.8) we get

$$Z_{DR} = 10 \log_{10} \left(\frac{3}{8}X^2 + \frac{1}{4}X + \frac{3}{8} \right), \quad \text{where} \quad X = \frac{1 + |\epsilon - 1|\,[1 - L_a]\,/2}{1 + |\epsilon - 1|L_a}. \tag{A.13}$$

For extremely prolate particles, $L_a \to 0$ and $Z_{DR} \to 10 \log_{10} \left[\left(3|\epsilon|^2 + 10|\epsilon| + 19 \right) /32 \right]$. This is the maximum possible Z_{DR} that can be obtained by solid ice columns and is around 4 dB.

REFERENCES

Bacon, N. J., Swanson, B. D., Baker, M. B., and Davis, E. J. 1998 Breakup of levitated frost particles. *J. Geophys. Res.*, **103,** 13 763–13 775.

Bader, M. J., Clough, S. A., and Cox, G. P. 1987 Aircraft and dual polarization radar observations of hydrometeors in light stratiform precipitation. *Q. J. R. Meteorol. Soc.*, **133,** 491–515.

Batten, L. J. 1973 *Radar observations of the atmosphere.* University of Chicago Press, Chicago.

Baumgardner, D., and Korolev, A. 1997 Airspeed corrections for optical array probe sample volumes. *J. Atmos. Oceanic Tech.*, **14,** 1224–1229.

Bower, K. N., Moss, S. J., Johnson, D. W., Choularton, T. W., Latham, J., Brown, P. R. A., Blyth, A. M., and Cardwell, J. R. 1996 A parametrization of the ice water content observed in frontal and convective clouds. *Q. J. R. Meteorol. Soc.*, **122,** 1815–1844.

Brown, P. R. A., and Francis, P. N. 1995 Improved measurements of the ice water content in cirrus using a total-water probe. *J. Atmos. Oceanic Tech.*, **12,** 410–414.

Chapman, D., and Browning, K. A.	1997	Radar observations of wind-shear splitting within evolving atmospheric Kelvin-Helmholtz billows. *Q. J. R. Meteorol. Soc.,* **123,** 1433–1439.
Chapman, D., and Browning, K. A.	1999	Release of potential shearing instability in warm frontal zones. *Q. J. R. Meteorol. Soc.,* **125,** 2265–2289.
Cho, H. R., Iribarne, J. V., and Richards, W. G.	1981	On the orientation of ice crystals in a cumulonimbus cloud. *J. Atmos. Sci.,* **38,** 1111–1115.
Cardwell, J. R., and Choularton, T. W.	2000	The importance of embedded convection and the Hallett Mossop process to the parameterisation of deep layer clouds. *Proc. 13th Int. Conf. on Clouds and Precip.,* 14–18 Aug. 2000, Reno, Nv., pp. 584–585.
Durran, D. R., and Klemp, J. B.	1982	On the effects of moisture on the Brunt-Väisälä frequency. *J. Atmos. Sci.,* **39,** 2152–2158.
Fletcher, N. H.	1962	*The Physics of Rainclouds.* Cambridge University Press, pp. 241.
Fowler, L. D., and Randall, D. A.	1996	Liquid and ice cloud microphysics in the CSU general circulation model. 3. Sensitivity to modeling assumptions. *J. Climate,* **9,** 561-586.
Gans, R.	1912	Über die Form ultramikroskopischer Goldteilchen (On the shape of ultra-microscopic gold particles). *Ann. Phys.,* **37,** 881–900.
Gardiner, B. A., and Hallett, J.	1985	Degradation of in-cloud forward scattering spectrometer probe measurements in the presence of ice particles. *J. Atmos. Sci.,* **2,** 171–180.
Gayet, J. F., Brown, P. R. A., and Albers, F.	1993	A comparison of in-cloud measurements obtained with 6 PMS 2D-C probes. *J. Atmos. Oceanic Tech.,* **10,** 180–194.
Goddard, J. W. F., Eastment, J. D., and Thurai, M.	1994	The Chilbolton Advanced Meteorological Radar: a tool for multi-disciplinary atmospheric research. *Electron. & Commun. Eng. J.,* **6,** 77–86.
Gregory, D., and Morris, D.	1996	The sensitivity of climate simulations to the specification of mixed phase clouds. *Climate Dynamics,* **12,** 641-651.
Griggs, D. J., and Choularton, T. W.	1986	A laboratory study of secondary ice particle production by the fragmentation of rime and vapour-grown ice crystals. *Q. J. R. Meteorol. Soc.,* **112,** 149–163.
Hall, M. P. M., Goddard, J. W. F., and Cherry, S. M.	1984	Identification of hydrometeors and other targets by dual-polarization radar. *Radio Sci.* **19,** 132–140.
Hallett, J., and Mossop, S. C.	1974	Production of secondary ice particles in the riming process. *Nature,* **249,** 26–28.
Herzegh, P. H., and Conway, J. W.	1986	On the morphology of dual-polarization radar measurements: Distinguishing meteorological effects from radar system effects. *Proc. 23rd AMS Conference on Radar Meteorology,* 22–26 Sept. 1986, Snowmass, Co., pp. 55–58.
Heymsfield, A. J.	1977	Precipitation development in stratiform ice clouds: a microphysical and dynamical study. *J. Atmos. Sci.,* **34,** 367–381.
Hobbs, P. V.	1974	High concentrations of ice particles in a layer cloud. *Nature,* **251,** 694–696.
Hobbs, P. V., and Rangno, A. L.	1985	Ice particle concentrations in clouds. *J. Atmos. Sci.,* **42,** 2523–2523.
Hogan, R. J., and Illingworth, A. J.	1999	A climatology of supercooled layer clouds from lidar ceilometer data. *CLARE'98 Final workshop, 13–14 September 1999* ESA/ESTEC, Noordwijk, The Netherlands, pp. 161–165.
Hogan, R. J., Illingworth, A. J., and Field, P. R.	1999	Polarimetric radar observations of the growth of highly-aligned ice crystals in the presence of supercooled water. *CLARE'98 Final workshop, 13–14 September 1999* ESA/ESTEC, Noordwijk, The Netherlands, pp. 167–171.
Illingworth, A. J., Goddard, J. W. F., and Cherry, S. M.	1987	Polarization radar studies of precipitation development in convective storms. *Q. J. R. Meteorol. Soc.,* **113,** 469–489.
Knollenberg, R. G.	1970	The optical array: An alternative to scattering for airborne particle size determination. *J. Appl. Meteorol.,* **9,** 86–103.
Korolev, A. V., Strapp, J. W., Isaac, G. A., and Nevzorov, A. N.	1998	The Nevzorov airborne hot-wire LWC–TWC probe: Principle of operation and performance characteristics. *J. Atmos. Oceanic Tech.,* **15,** 1495–1510.
Korolev, A. V., Isaac, G. A., and Hallett, J.	2000	Ice particle habits in stratiform clouds. *Q. J. R. Meteorol. Soc.,* **126,** 2873–2902.
Lalas, D. P., and Einaudi, F.	1974	On the correct use of the wet adiabatic lapse rate in stability criteria of a saturated atmpsphere. *J. Appl. Meteorol.,* **13,** 795–800.

Liebe, H. J., Manabe, T., and Hufford, G. A.   1989   Millimeter-wave attenuation and delay rates due to fog/cloud conditions. *IEEE AP,* **37,** 1617–1623.

Liou, K.-N.   1986   Influence of cirrus clouds on weather and climate processes: A global perspective. *Mon. Weath. Rev.,* **114,** 1167–1199.

Liu, J.-L., and Herzegh, P. H.   1986   Differential reflectivity signatures in ice-phase precipitation: Radar-aircraft comparisons. *Proc. 23rd AMS Conference on Radar Meteorology,* 22–26 Sept. 1986, Snowmass, Co., pp. 59–61.

Mason, B. J.   1998   The production of high ice-crystal concentrations in stratiform clouds. *Q. J. R. Meteorol. Soc.,* **124,** 353–356.

Meneghini, R., and Liao, L.   1996   Comparisons of cross-sections for melting hydrometeors as derived from dielectric mixing formulas and a numerical method. *J. Appl. Met.,* **35,** 1658–1670.

Mitchell, D. L.   1996   Use of mass- and area-dimensional power laws for determining precipitation particle terminal velocities. *J. Atmos. Sci.,* **53,** 1710–1723.

Moss, S. J., and Johnson, D. W.   1994   Aircraft measurements to validate and improve numerical model parametrizations of ice to water ratios in clouds. *Atmos. Res.,* **34,** 1–25.

Mossop, S. C., and Hallett, J.   1974   Ice crystal concentration in cumulus clouds: influence of the drop spectrum. *Science,* **186,** 632–634.

Oraltay, R. G., and Hallett, J.   1989   Evaporation and melting of ice crystals: a laboratory study. *Atmos. Res.,* **24,** 169–189.

Pruppacker, H. R., and Klett, J. D.   1997   *Microphysics of clouds and precipitation.* 2nd Ed., Kluwer Academic Publishers, 954 pp.

Sauvageot, H., Kouadio, K., and Etty, C.   1986   The influence of temperature and supersaturation on the polarization of radar signals. *Proc. 23rd AMS Conference on Radar Meteorology,* 22–26 Sept. 1986, Snowmass, Co., pp. 173–176.

Seliga, T. A., and Bringi, V. N.   1976   Potential use of radar differential reflectivity measurements at orthogonal polarizations for measuring precipitation. *J. Appl. Met.,* **15,** 69–76.

Smith, R. N. B.   1990   A scheme for predicting layer clouds and their water content in a general circulation model. *Q. J. R. Meteorol. Soc.,* **116,** 435–460.

Sundqvist, H.   1993   Inclusion of ice phase of hydrometeors in cloud parameterization for mesoscale and largescale models. *Beitr. Phys. Atmos.,* **66,** 137–147.

Tremblay, A., Glazer, A., Yu, W., Benoit, R.   1996   A mixed-phase cloud scheme based on a single prognostic equation. *Tellus A,* **48,** 483–500.

van de Hulst, H. C.   1957   *Light scattering by small particles.* Wiley, New York.

Vardiman, L.   1978   The generation of secondary ice particles in clouds by crystal collision. *J. Atmos. Sci.,* **35,** 2168–2180.

Wilson, D. R., and Ballard, S. P.   1999   A microphysically based precipitation scheme for the UK Meteorological Office Unified Model. *Q. J. R. Meteorol. Soc.,* **125,** 1607–1636.